Materials Characterization 167 (2020) 110466

Contents lists available at ScienceDirect

Materials Characterization

journal homepage: www.elsevier.com/locate/matchar

Effects of C/Si ratios on structures and behaviors of NbSiCN nanocomposite films synthesized by reactive magnetron sputtering

Haoming Du[a,b], Ping Liu[a], Wei Li[a,*], Ke Zhang[a], Fengcang Ma[a], Xiaohong Chen[a], JunWei Yang[b], Rui Feng[c], Peter K. Liaw[c,*]

[a] School of Materials Science and Engineering, University of Shanghai for Science and Technology, Shanghai 200093, PR China
[b] School of Materials Science and Engineering, Shanghai Dianji University, Shanghai 200240, PR China
[c] Department of Materials Science and Engineering, The University of Tennessee, Knoxville, TN 37996, USA

ARTICLE INFO

Keywords:
NbSiCN nanocomposite film
Interfaces
Microstructure
Interface coherency
Superhardness effect
Two-way doped mechanism

ABSTRACT

A variety of quarternary NbSiCN nanocomposite films, which with the different Si and Ni contents, are deposited on Si (100) substrates by the reactive magnetron sputtering. The X-ray diffraction, field-emission scanning electron microscopy, high-resolution transmission electron microscopy, X-ray photoelectron spectroscopy, nanoindentation techniques, and substrate curvature methods were used to research the effects of C/Si contents ratio on the microstructures and mechanical behaviors of the NbSiCN nanocomposite films. The fabrication of the NbSiCN nanocomposite film can be described as a two-way doped mechanism. When the C/Si content ratio was 1: 4 or 3:2, the films showed the best crystallinity with the pronounced preferential (111) and (200) orientations, respectively. Meanwhile, the corresponding $Nb_{20}Si_4C_1N$ and $Nb_{20}Si_2C_3N$ presented two equally-low values of average crystallite sizes and obvious optimal mechanical properties. The first-principles calculation was utilized to obtain Young's modulus of the interfacial layer, which was difficult to obtain the values by experiments. The combined effects of the modulus-difference and alternating-stress-field strengthening mechanisms, and Hall-Petch relationship produce the hardness effect of the NbSiCN nanocomposite film, which is composed of the interfacial layer of numerous compounds.

1. Introduction

Over the past decades, the nanocomposite films have triggered the concerns of many researchers, because these films universally exhibit enhanced mechanical properties in contrast to their constituent materials [1–3]. It can artificially obtain superhard thin films by such superhardness effects. The nanocomposite films are composed of nanocrystallites ($\leq$10 nm) encapsulated by interfacial layers, which can be categorized into two categories according to the type of the interfacial layer. The first type is the film with an interfacial layer of the compound. The second one is the film with an interfacial layer of the metal.

Currently, the nanostructure and strengthening mechanism of the first typological nanocomposite films have been extensively interpreted by the "nc-TmN/a-Si_3N_4" model proposed by Veprek et al. in 1995 [4], in which equiaxed TmN (transition metal nitride) nanocrystallites (nc-TmN) were encapsulated in an amorphous Si_3N_4 (a-Si_3N_4) interface. But due to the lack of the competent and immediate experimental evidence, the "nc-TmN/a-Si_3N_4" model still remains controversial [5,6]. Especially, our recent research found an important phenomenon in the TiSiN and TiAlSiN nanocomposite films, which were strengthened with an appropriate Si content, as follow [7]. Firstly, the Si_3N_4 interfacial phase can be crystallized between adjacent TiN and TiAlN nanocrystallites, which does not agree with the "nc-TmN/a-Si_3N_4" model. Secondly, the columnar growth structure could coexist with the nanocomposite structure within a Ti(*Al*)SiN film.

The coherent-interface-strengthening mechanism can be still applied to the second type of nanocomposite films. For example, our recent research found that when TiNiN nanocomposite films were strengthened with a proper Ni content, the Ni interfaces could coordinate the misorientations between TiN nanocrystallites. At the same time, the Ni interfaces could also grow coherently with the adjacent TiN nanocrystallites [8]. The phenomenon suggested that the nc-TmN/a-Me model was not suitable for the TiNiN nanocomposite films, but the coherent interface mechanism was appropriate.

Because of the thermodynamic incompatibility, the NbSiN films are regarded as having a typical nanocomposite structure with an interfacial phase of Si_3N_4 [9–11]. With the development of the dry and high-speed cutting technology, more complex films, compared with ternary

* Corresponding authors.
E-mail addresses: liwei176@usst.edu.cn (W. Li), pliaw@utk.edu (P.K. Liaw).

https://doi.org/10.1016/j.matchar.2020.110466
Received 4 May 2020; Received in revised form 25 June 2020; Accepted 25 June 2020
Available online 29 June 2020

nanocomposite films, have been designed to further promote the mechanical properties and thermal stabilities [12], e.g., TiSiCN [13–15], TiZrAlN [16,17], CrMoSiN [18,19], TiNbSiN [20], and AlMgBTi [21]. But regrettably, the hardness effects of those nanocomposite films were just simply explained by the "nc-TmN/a-Si3N4" model [4], which may not reveal the strengthening mechanisms of those nanocomposite films. It is worth further investigations whether the coherent-interface-strengthening mechanism can be applied to the nanocomposite film with the interfacial layer of two and more compounds or not. For this purpose, the quarternary NbSiCN nanocomposite films are deposited by a reactive-magnetron synthesized technique, which with the different C and Si contents. The influences of the different C and Si contents on the microstructures and mechanical properties of the NbSiCN nanocomposite films would be studied. Particular attention would be used to the interfacial morphology through the direct experimental method when the film is strengthened with appropriate C and Si contents, which is to elucidate the strengthening mechanism of the NbSiCN nanocomposite film.

2. Material and methods

2.1. Fabrication of films

The reactive-magnetron sputtering system was used to fabricate the NbSiCN nanocomposite films, $Nb_{20}Si_5N$ and NbCN nanostructured films on the Si(100) substrates at room temperature. The NbSiCN films, $Nb_{20}Si_5N$ and NbCN films were sputtered from the NbSiC compound target [99.99, atomic percent (at.%)], $Nb_{20}Si_5$ compound target (99.99 at.%), and NbC compound target (99.99 at.%) with a diameter of 75 mm, respectively. The power was maintained at 300 W by a radio-frequency (RF) mode. The pure Nb (99.99 at.%), Si (99.99 at.%), and C targets (99.99 at.%) were respectively cut into 25 pieces to fabricate the NbSiC compound targets with different Si and C contents. Because of the total amount of Si and C has an important effect on the NbSiCN nanocomposite films, the number of Si and C was fixed at 5 in the present research. The NbSiC compound targets with different C:Si:Nb volume were fabricated by replacing different pieces of Si and C. The C:Si:Nb volume was set at 0:5:20, 1:4:20, 2:3:20, 3:2:20, 4:1:20, and 5:0:20, respectively. As mentioned above, the NbC compound targets with different C contents were also fabricated by replacing different pieces of Nb with the same piece of C. The NbC targets with different C/Nb volumes, including 0:25, 1:24, 2:23, 3:22, 4:21, and 5:20, were fabricated, respectively. For the purpose of avoiding contamination, the background pressure was pumped down to 5.0×10^{-4} Pa before the deposition. The high-purity N_2 (99.999 at.%) and Ar (99.999 at.%) were introduced into the chamber, and the N_2 and Ar flow rates were kept at 5 and 38 sccm (standard-state cubic centimeter per minute), respectively. The total working pressure was kept at 6.0×10^{-1} Pa. Before the reactive magnetron sputtering, the Si substrates were ultrasonically cleaned in alcohol and acetone for 10 min, respectively. The Si substrates were then mounted on a rotating substrate holder in a vacuum chamber. The distance between the substrate and target was 50 mm. Before the deposition of the NbSiCN nanocomposite films, the Si substrates were subjected to further sputtering for 15 min for the pretreatment. In order to improve the homogeneity of films, the substrate rotation was set at a speed of 10 r/min. The deposition time for each sample and the thickness of each film were summarized in Table 1.

2.2. Characterizations and measurements

The crystal structures of the films were examined by means of X-ray diffraction (XRD) using a Bruker D8 Advance system with the Cu K_α radiation. The step time and size for XRD were set at 5 s and 0.02°, respectively. The XRD measurements were implemented in the Bragg-Brentano (θ/2θ) scan mode with operating parameters of 20 mA and 30 kV. The diffraction angles (2θ) were scanned from 20° to 90°. In the investigation of the selected reflection of the NbSiCN nanocomposite films, the grain sizes of the films (D) were calculated, using the Scherrer formula [22].

Table 1
The deposition time and thickness of all the NbSiCN films.

Film	Deposition time (s)	Thickness (μm)
$Nb_{20}Si_5N$	7200	2.2
$Nb_{20}Si_4C_1N$	7200	1.9
$Nb_{20}Si_3C_2N$	7200	2.1
$Nb_{20}Si_2C_3N$	7200	2.0
$Nb_{20}Si_1C_4N$	7200	2.2
$Nb_{20}C_5N$	7200	2.1

$$D = 0.89\lambda/(B\cdot\cos\theta) \quad (1)$$

where D is the average crystallite size perpendicular to the reflecting planes, λ is the x-ray wavelength, B is the half-width of the peak in radians due to the finite size of the crystal, and θ is the Bragg angle. The chemical compositions of the NbSiCN nanocomposite films were determined by energy dispersive spectroscopy (EDS) on a Philips Quanta FEG450. The microstructures of the NbSiCN nanocomposite films were investigated by the field-emission high-resolution transmission electron microscopy (HRTEM), using a Philips CM200-FEG instrument. The X-ray photoelectron spectroscopy (XPS, Kratos AXIS Ultra DLD) was utilized to analyze the bonding structure, with an Al-K_α ($h\nu$ = 1486.6 eV) radiation source operated at 150 W.

The hardness and elastic modulus of the films were measured on an Agilent G200 nanoindenter equipped with a Berkovich diamond indenter, using the Oliver and Pharr method [23]. The surveys were implemented by applying a load of 5 mN at a rate of 0.1/s. At the same time, the indentation depth was approximately set at 100 nm, which was less than 1/10th of the film thickness, to minimize the effect of the substrate on the measurements. Each value of mechanical properties was an average of at least 16 measurements. The residual stresses of the films were studied by the substrate curvature methods, using a SuPro Film Stress Tester FST1000 instrument. In the investigation of the wafer curvature of the NbSiCN nanocomposite films, the residual stresses of the films were calculated, using the Stoney formula [24]. The relationship between the average stress in the film and the variation of the curvature of the film-substrate system is revealed by Stoney equation.

$$\sigma_f = \frac{h_s^2 E_s}{6(1-\nu)h_f}\left(\frac{1}{R_2} - \frac{1}{R_1}\right) \quad (2)$$

where h_s is the thickness of the substrate, E_s is the Young's modulus of the Si substrate, h_f is the thickness of the nanocomposite film, ν is the Poisson's ratio of the Si substrate, R_1 and R_2 are the radii of the substrate before and after sputtering.

3. Model and computational details

The process for calculating the hardness increment of the NbSiCN nanocomposite film is described as follows. Firstly, the primitive lattice constants of a, b, c, atomic coordinates, type and number of the new super-crystal cell, and distribution of the replaced atoms are given. Subsequently, the model of the new super-crystal cell and Young's modulus are calculated by the first-principles calculations. The shear moduli of the new super-crystal cell are calculated according to the Young's modulus. And then, the hardness increment is calculated according to the modulus-difference theory [25], alternating-stress-field theory [26], and Hall-Petch relationship [27,28], respectively. Finally, the total theoretical hardness is obtained by the above data.

The first-principles calculation was performed, based on the density functional theory. The crystal structure of the nanomonolayer face-centered-cubic (fcc)-structured NbN composed of four atoms of

niobium (Nb) and four atoms of nitrogen (N). Based on the coherent interface growth in the $Nb_{20}Si_2C_3N$ nanocomposite film, the models of the $Si_3N_4/C/CN_x$ interfacial layer in $Nb_{20}Si_2C_3N$ were built by replacing corresponding atoms in the fcc-structured NbN crystal cell with atoms of carbon and silicon, which could be described as a $C_9Si_6N_9$ super-crystal cell.

In the building of the $C_9Si_6N_9$ super-crystal cell model, the primitive unit cell with lattice constants of a = b = c = 0.3114 nm was used. The atomic coordinates were + 4 Nb (0,0,0) and + 4 N (0.5,0.5,0.5) in each model of the fcc-structured NbN crystal cell, respectively. Meanwhile, it replaces six atoms of niobium with six atoms of silicon, and also replaces six atoms of niobium and three atoms of nitrogen with nine atoms of carbon, respectively. For improving the calculation efficiency and considering the effect of the cyclic-boundary condition, the replacement of atoms is considered as a symmetric distribution of atoms.

The first-principles calculation was performed with the framework of the density functional theory (DFT) [29,30], using Vanderbilt-type ultrasoft pseudopotentials [31], as implemented in the Cambridge Serial Total Energy Package (CASTEP) code [32–34]. In the aspect of the plane-wave basis set, the cut-off energy was set at 310 eV. The Monkhorst-Pack method [35], which with a 5 × 5 × 5 k-point mesh, was used to carry out the k points sampling integration over the Brillouin zone. The exchange-correlation potential of the generalized gradient approximation (GGA) with the Perdew-Wang (PW91) [36] parametrization was employed. The geometry optimization adopted the Brodyden-Fletcher-Goldfarb-Shanno (BFGS) minimization scheme [37]. As the total energy is 2.0×10^{-6} eV/atom, the self-consistency was considered to be converged. The maximum value of the ionic Hellmann-Feynman force was set as 0.05 eV/Å. By setting the above parameters, the total energy and Young's modulus calculations could be well-converged in a good shape.

4. Experimental results

4.1. Microstructures

Fig. 1 shows the XRD patterns of NbSiCN nanocomposite films with the different Si and Ni contents. It can be seen that there are diffraction peaks of the crystalline NbN located at (111), (200), and (220) crystal planes [38–40]. No signals from the crystalline Si_3N_4 and C can be observed, which implied that the content of the interface phase was low in nanocomposite films. As the C/Si content ratio is 5:0, the film only

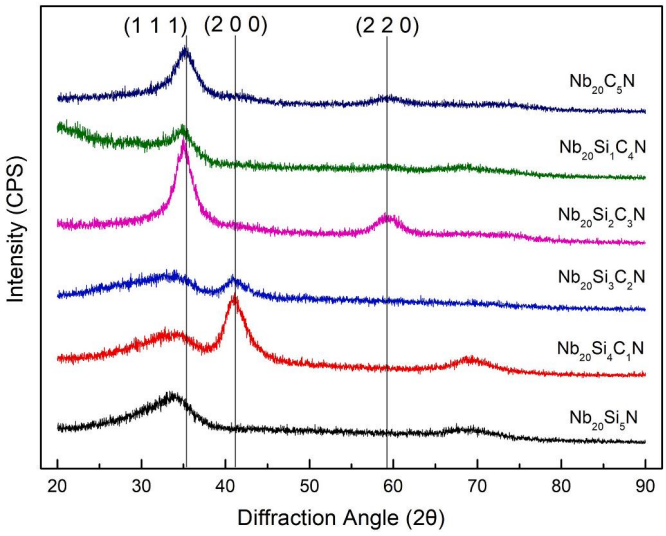

Fig. 1. XRD patterns of NbSiCN nanocomposite films with the different C/Si ratios.

reveals an obvious diffraction peak located at the (111) orientation. Because of the absence of the Si element, the NbCN film cannot form the nanocomposite structure [41]. To reduce the energy in the fcc structure, the NbCN film tends to grow along the (111) crystal plane [42].

After the initial insertion of the Si elements, the intensity of the (111) diffraction peak descends. The appearance shows that the crystallization degree of the film decreases. This phenomenon also proves that the NbCN-nanostructured film does not form nanocomposite structures with coherent interfaces under the present preparation condition. As the C/Si content ratio further decreases to 3:2, the intensity of the (111) diffraction peak increases again and reaches the maximum, suggesting that the $Nb_{20}Si_2C_3N$ film develops the highest crystallization degree with a (111) preferential orientation. At the same time, the (220) peak can be observed in the $Nb_{20}Si_2C_3N$ film.

As the C/Si ratio declines from 3:2 to 1:4, the intensity of the (111) peak becomes gradually weak, and the intensity of the (200) diffraction peak remarkably increases. It indicates that the film crystallinity is with a prominent (200) preferential orientation. When the C/Si content ratio is 0:5, the preferred orientation of the film changes from (200) to (111) orientations, and the diffraction intensity decreases.

In order to determine the C/Si ratio before and after sputtering, EDS is used to determine the chemical compositions of the NbSiCN nanocomposite films. The C/Si ratios of the NbSiCN nanocomposite films are shown in Table 2. Because of the oxygen concentration is lower than 2 at.% in all films, it is disregarded in the quantification. The detection of oxygen is likely caused by the residual organic substance in the vacuum chamber or contaminants on the coating surface. The C/Si ratio after sputtering is slightly lower than that before sputtering. The deviation of them is increased with the C element increasing. The most important reason for this phenomenon is likely due to the Si substrates for every films.

Because of the maximum of the crystallization degree with a pronounced preferential (111) orientation, the typical cross-sectional HRTEM images and selected area electron diffraction (SAED) patterns of the $Nb_{20}Si_2C_3N$ film are exhibited in Fig. 2. From the low-magnification image of Fig. 2(a), it can be clearly seen that the $Nb_{20}Si_2C_3N$ film presents an obvious columnar growth structure, which is similar to the NbN monolithic film. The columnar growths are indicated in Fig. 2(a) by red arrows. Moreover, the medium-magnification image of the red dashed line area in Fig. 2(b) indicates that some dark nano-sized grains exist in an individual columnar grain.

Fig. 2(c) shows the highly-magnified morphology of the nanocomposite structure. The yellow a, b, c, d, e, and f are used to mark the interfaces between the adjacent nanocrystallites. Meanwhile, there exist the NbN nanocrystallites with the dark contrast marked by the red A, B, C, D, E, F and G, which were surrounded by the interfaces. The nanocomposite structure can be clearly observed in the NbSiCN film with the C/Si content ratios of 3:2 and with the equiaxed nanocrystallites surrounded by the interfaces. In Fig. 2(d), the SAED patterns indicate that the $Nb_{20}Si_2C_3N$ film exhibits an fcc structure with the (111) preferred orientation, which are in agreement with the XRD data in Fig. 1. When the C/Si ratio declines to 1:4, the film shows the highest crystallization degree with a pronounced (200) preferential orientation. Fig. 3 presents the typical cross-sectional HRTEM images and SAED patterns of the $Nb_{20}Si_4C_1N$ film. The columnar growth structure still can be observed in the $Nb_{20}Si_4C_1N$ film from Fig. 3(a). The columnar growths are indicated in Fig. 3(a) by red arrows. As shown in the magnified image presented in the red dashed line area from Fig. 3(b), an obvious nanocomposite structure is created in the $Nb_{20}Si_4C_1N$ film with the dark nanocrystallites surrounded by the bright interfaces. The interface can still be found in the crystallized state of the NbSiCN film with the C/Si content ratio of 1:4, as illustrated in Fig. 3(c). Furthermore, the lattice fringes of NbN nanocrystallites denoted by the red A, B, C, D, E, and F are surrounded by crystallized interfaces with the bright contrast marked by the yellow a, b, c, d, e, and f, as shown in Fig. 3(c),

Table 2
The C/Si ratio before and after sputtering.

Sample	Amount of C chips on target	Amount of Si chips on target	C/Si ratio before sputtering	C (at.%)	Si (at.%)	C/Si ratio after sputtering	Deviation (%)
$Nb_{20}Si_5N$	0	5	0:5	0	23.9	0:23.9	/
$Nb_{20}Si_4C_1N$	1	4	1:4	4.7	20.7	4.7:20.7	9.2
$Nb_{20}Si_3C_2N$	2	3	2:3	11.0	18.6	11.0:18.6	11.3
$Nb_{20}Si_2C_3N$	3	2	3:2	14.3	11.2	14.3:11.2	14.9
$Nb_{20}Si_1C_4N$	4	1	4:1	19.1	5.9	19.1:5.9	19.1
$Nb_{20}C_5N$	5	0	5:0	22.7	0	22.7:0	/

suggesting that the nanocomposite film is incompatible with the "nc-nanocrystallite/a-interface" model. Compared to Fig. 2(d), Fig. 3(d) still indicates the legible SAED patterns, whereas the $Nb_{20}Si_4C_1N$ film exhibits an fcc structure with the (200) preferred orientation. From the images of Figs. 2 and 3, the interface coherency and nanocomposite structures in both the $Nb_{20}Si_2C_3N$ and $Nb_{20}Si_4C_1N$ nanocomposite films can be observed. Meanwhile, the $Nb_{20}Si_2C_3N$ nanocomposite film is better than the $Nb_{20}Si_4C_1N$ nanocomposite film in both the film crystallinity and the interface coherency. The above two results are also in accordance with the XRD data shown in Fig. 1.

The chemical bonding states in the $Nb_{20}Si_2C_3N$ and $Nb_{20}Si_4C_1N$ nanocomposite films are examined to identify the phase structures of the nanocrystallites and interfaces. Figs. 4 and 5 demonstrate the XPS spectra taken in the Si 2p, N 1s, and C 1s energy regions for the $Nb_{20}Si_2C_3N$ and $Nb_{20}Si_4C_1N$ nanocomposite films, respectively. The Si_3N_4 phase can be identified by a peak at 101.7 eV in the Si 2p spectrum [43]. The Ni 1s peaks are presented in the Figs. 4(b) and 5(b), where the peaks corresponding to 399.7 eV, 397.5 eV, and 396.7 eV are in agreement with the binding energies of CN_x [44], Si_3N_4 [45], and NbN [46,47], respectively. The C 1s spectra for both $Nb_{20}Si_2C_3N$ and $Nb_{20}Si_4C_1N$ nanocomposite films show a main peak and a weak peak at 284.8 eV and 285.2 eV, respectively. These peaks correspond to a major component of C—C [48] and a smaller component C—N [49].

From the results of the above-mentioned studies of XRD, HRTEM, and XPS, it can be concluded that both $Nb_{20}Si_2C_3N$ and $Nb_{20}Si_4C_1N$ nanocomposite films are characterized as the nanocomposite structures. The NbN nanocrystallites are surrounded by the interface phase, which is constituted of Si_3N_4, C, and trace amounts of CN_x, in both $Nb_{20}Si_2C_3N$ and $Nb_{20}Si_4C_1N$ nanocomposite films. The collected experimental data reflect that the effects of C and Si contents on the interface of the

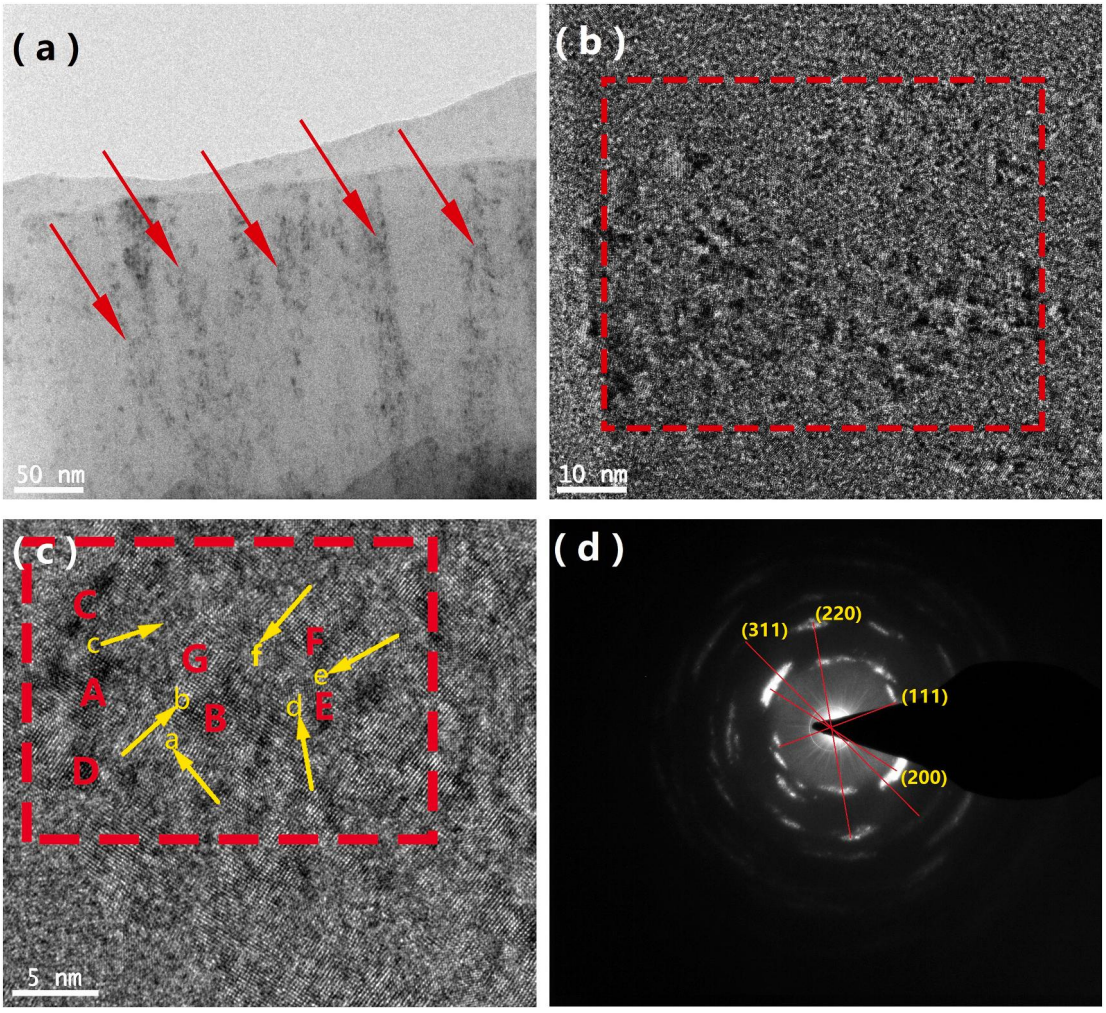

Fig. 2. Cross-sectional HRTEM images of the $Nb_{20}Si_2C_3N$ nanocomposite film: (a) low-magnification, (b) medium-magnification, (c) high-magnification, and (d) selected area diffraction patterns.

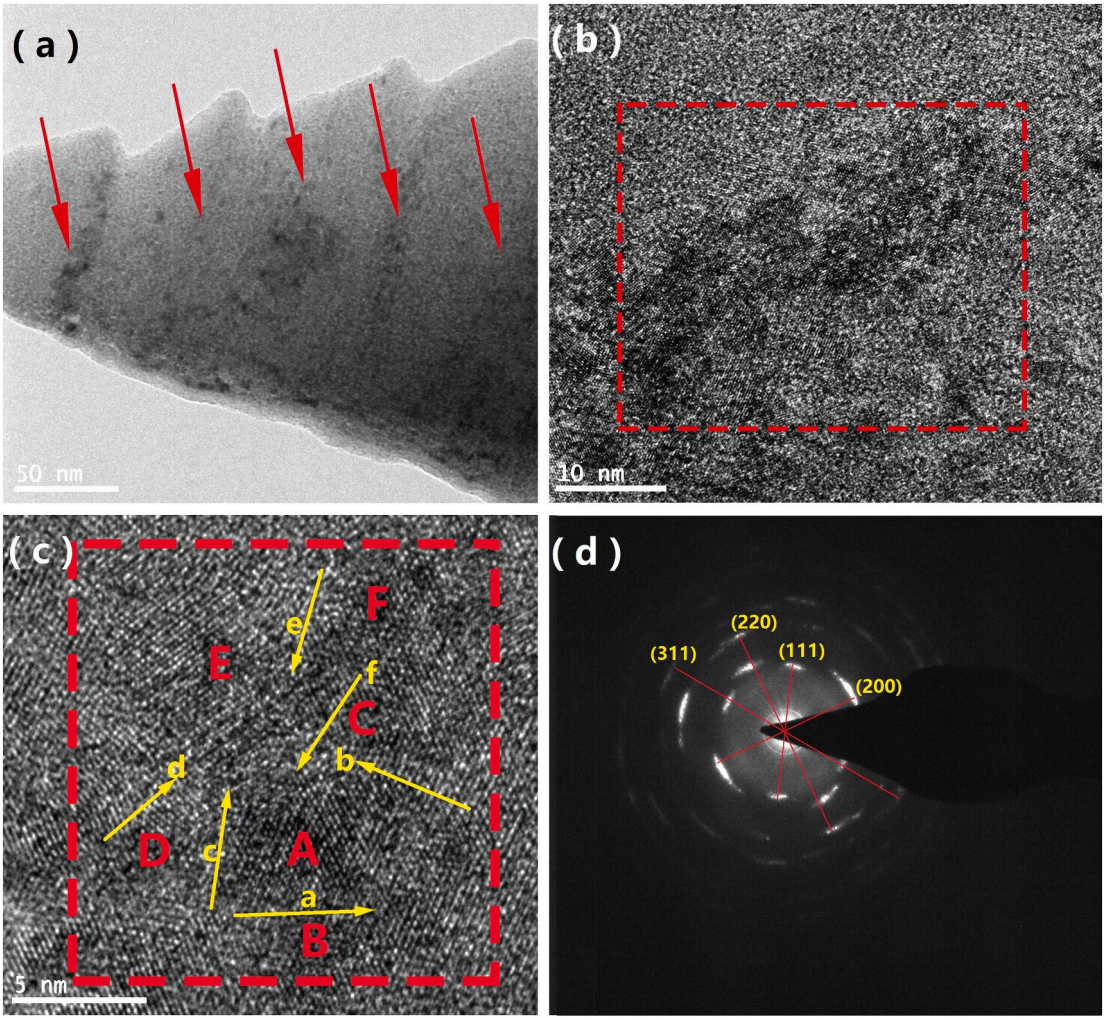

Fig. 3. Cross-sectional HRTEM images of the $Nb_{20}Si_4C_1N$ nanocomposite film: (a) low-magnification, (b) medium-magnification, (c) high-magnification, and (d) selected area diffraction patterns.

NbSiCN nanocomposite film are similar to those on the interface of TiSiCN [50]. The C and CN_x dissolve into the interface, and combine with Si_3N_4 to form the $Si_3N_4/C/CN_x$ interface phase.

4.2. Mechanical properties

Fig. 6 exhibits the dependence of the hardnesses and elastic moduli of NbSiCN nanocomposite films with the change of the C/Si content ratio. When no Si is added in the film, the maximum hardness and elastic modulus of the NbCN nanostructured film are 26.1 GPa and 297.5 GPa, respectively. After the initial addition of the Si element, the corresponding values for the $Nb_{20}Si_1C_4N$ nanostructured film deposited under the same conditions first decrease to 24.7 GPa and 240.5 GPa. In the $Nb_{20}Si_2C_3N$ nanocomposite film, the addition of the Si element leads to the increase of the hardness and elastic modulus of the nanocomposite film, which reach the high values of 32.5 GPa and 344.8 GPa, respectively. But, with further increasing the Si content, the mechanical properties rapidly decrease to the minimum values. As the C/Si content ratio reaches 1:4, the mechanical properties of the NbSiCN nanocomposite film improve again, and the maximum hardness and elastic modulus are 35.0 GPa and 344.1 GPa, respectively. However, in the NbSiN nanostructured film, the hardness and elastic modulus values

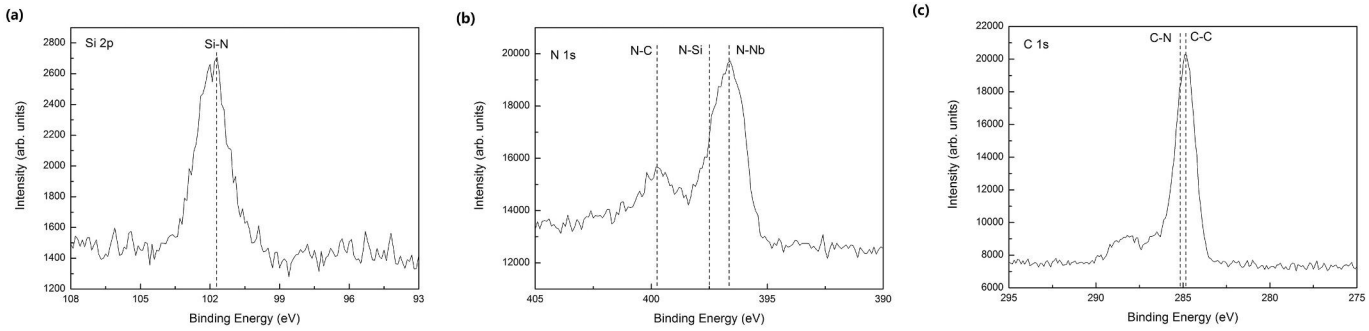

Fig. 4. XPS spectra of the $Nb_{20}Si_2C_3N$ nanocomposite film: (a) Si 2p, (b) N 1s, and (c) C 1s.

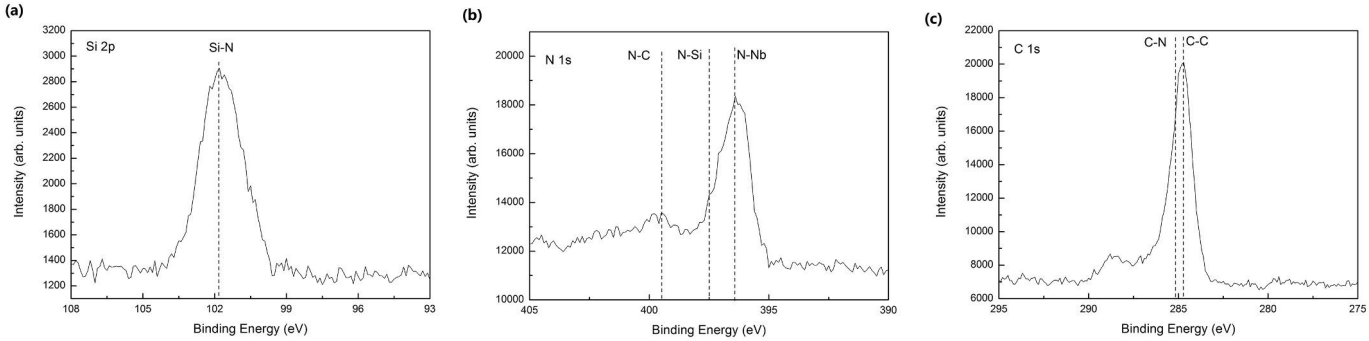

Fig. 5. XPS spectra of the $Nb_{20}Si_4C_1N$ nanocomposite film: (a) Si 2p, (b) N 1s, and (c) C 1s.

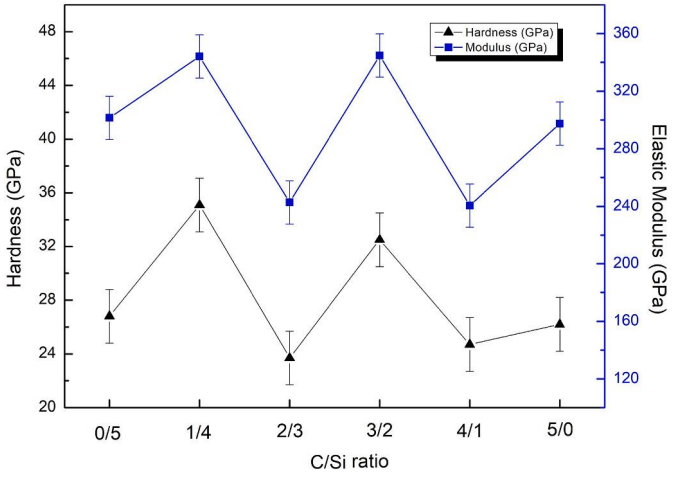

Fig. 6. Variation of hardnesses and elastic moduli of NbSiCN nanocomposite films with the change of the C/Si ratio.

rapidly decrease to 26.7 GPa and 301.5 GPa, respectively.

It is interesting to see a double peak graph according to the variation of the hardnesses and elastic moduli of NbSiCN nanostructured films with the C/Si content ratio. Two hardness peaks and two elastic modulus peaks in Fig. 7 are in agreement with XRD patterns, which own high crystallinities with the pronounced preferential (111) and (200) orientations, respectively.

To analyze the strengthening mechanism of NbSiCN nanocomposite films, Fig. 7 shows the dependence of hardnesses and elastic moduli of the NbCN nanostructured films on the C content. Under the same

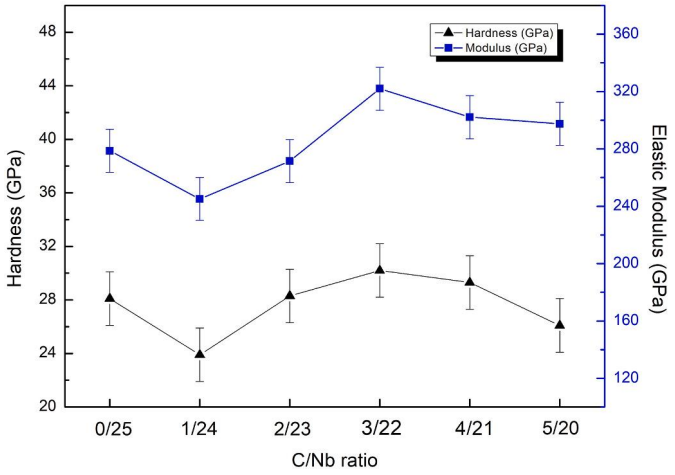

Fig. 7. Variation of hardness and elastic modulus of the NbCN nanostructured film with the change of the C content.

fabrication conditions, the hardness and elastic modulus of the NbN film were measured as 28.1 GPa and 278.6 GPa, respectively. After the initial insertion of the C content (C/Nb = 1:24), the hardness and elastic modulus of the nanostructured films first decrease to 23.9 GPa and 245.1 GPa, respectively. However, with an increase in the C content, the mechanical properties of the nanostructured films gradually improve. In the $Nb_{22}C_3N$ nanostructured film, the maximum hardness and elastic modulus are 30.2 GPa and 321.9 GPa, respectively. When the C content further increases, however, the mechanical properties values gradually decrease again.

Fig. 8 shows the residual stress of the NbSiCN nanocomposite films with different C/Si content ratios. It can be seen that the variation of the residual stresses is similar to that of the hardnesses and elastic moduli. The residual stresses show significant increases in both $Nb_{20}Si_2C_3N$ and $Nb_{20}Si_4C_1N$ nanocomposite film, which the values are 0.52 GPa and 0.47 GPa, respectively.

5. Discussion

5.1. Microstructural evolution of NbSiCN films with the change of the C/Si ratio

The D values for the NbSiCN nanocomposite films with different C/Si content ratios using the Scherrer equation [22] are summarized in Table 3. It can be seen that there are two decreases in the average crystallite sizes of the NbSiCN nanocomposite films with different C/Si content ratios. The D value for the $Nb_{20}Si_5N$ nanocomposite film is larger than those of the NbSiCN nanocomposite films. It can be seen

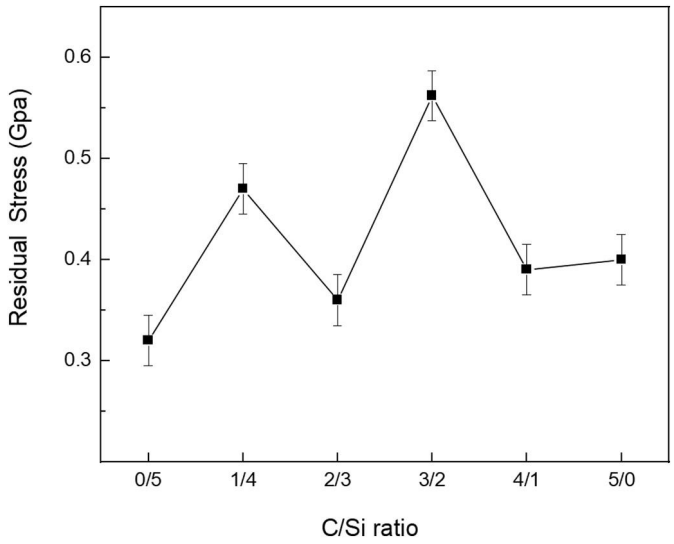

Fig. 8. Variation of residual stress of NbSiCN nanocomposite films with the change of the C/Si ratio.

Table 3
Average crystallite size (D) of the NbSiCN nanocomposite films with different C/Si content ratios calculated by the Scherrer Equation.

Film	C/Si content ratio	D (nm)
$Nb_{20}Si_5N$	0:5	45.3
$Nb_{20}Si_4C_1N$	1:4	10.0
$Nb_{20}Si_3C_2N$	2:3	19.1
$Nb_{20}Si_2C_3N$	3:2	11.2
$Nb_{20}Si_1C_4N$	4:1	15.1
$Nb_{20}C_5N$	5:0	10.7

that the film crystallites are refined with the insertion of C elements. With the initial insertion of C elements, the average crystallite size first decreases, and the $Nb_{20}Si_4C_1N$ nanocomposite film exhibits the minimum crystallite size of 10.0 nm. As the C/Si content ratio increases to 2:3, the average crystallite size rises to 19.1 nm. When the C/Si content ratio is 3:2, the D value declines to 11.2 nm. With the C/Si content ratio continued to increase, the D value rises and reaches the second maximum in the $Nb_{20}Si_1C_4N$ nanocomposite film. As no Si is inserted in the film, the D values decrease to 10.7 nm in the NbCN film.

Combined with the previous characterization and measurement, two minimum values of average crystallite sizes both exist in the NbSiCN nanocomposite films, which meanwhile show the highest crystallization degree with different preferential orientations. It can draw such a conclusion that the hardness effect of the NbSiCN nanostructured film can be explained by the combined actions of the coherent-interface-strengthening mechanism and the Hall-Petch relation theory.

In this investigation, XRD, SAED and XPS are the main methods of determining the chemical composition of the phases. From Fig. 1, it can be seen that all the films are only composed of NbN phases, while no other phase is detected. In Fig. 2(d) and Fig. 3(d), the SAED patterns indicate that the phases are in agreement with the XRD data in Fig. 1. In order to make the chemical composition of the phases more clearly, the XPS spectra are taken in the Si 2p, N 1s, and C 1s energy regions. In Figs. 4 and 5, the C—N and C—C bonds are observed in the spectra. At the same time, there is no C—Nb bond can be found in C 1s peaks. The results indicate that the C element exists as C and a small quantity of CN_x. There is no NbC or NbCN phase during the preparation. Compare with the gas sources used in the CVD techniques, the Nb and C from the solid NbSiC compound targets own lower activities. It is the main cause of the absence of NbC and NbCN phases in this investigation. The N—Nb bonds are observed in N 1s peaks, suggesting that NbN phase is created during the deposition. This phenomenon is in agreement with the results of XRD and SAED. The Si—N bonds are observed in Si 2p and N 1s peaks, suggesting that Si element exists as Si_3N_4.

5.2. Strengthening mechanisms

Based on the above discussion, the rise in the mechanical properties of the NbSiCN nanocomposite film can be explained by the combined actions of the coherent-interface-strengthening mechanism, and the Hall-Petch relation theory.

The fabrication of the NbSiCN nanocomposite film can be described below, which is a two-way doped mechanism. On one hand, it is a preparation of the Si-doped NbN film in the depositing process. On the other hand, it can be comprehended as a C-doped NbN film during the reactive sputtering. In the first case, the Si_3N_4 can hardly dissolve into the NbN nanocrystallites but solute into the interface. So the interface phases are combined with C and CN_x to form the $Si_3N_4/C/CN_x$. A similar phenomenon has also occurred in the second case. From the data of Fig. 7, the hardnesses of NbCN nanostructured films first increase and then gradually decline with the increase of C elements. The effect of the C content on properties of NbCN nanostructured films is illustrated in Fig. 9(a). In our previous investigation on NbSiN nanocomposite films [51], the hardness of NbSiN nanocomposite films also first increases and then gradually declines, as presented in Fig. 9(b). When the C and Si are mutually doped, the hardness effects from the C and Si can be accumulated, leading to a “double peak” hardness effect, which occurs in the $Nb_{20}Si_2C_3N$ and $Nb_{20}Si_4C_1N$ nanocomposite films, respectively, as exhibited in Fig. 9(c).

The microstructural evolution of the NbSiCN nanostructured film, which with increasing the C/Si content ratio from 0:5 to more than 3:2, is illustrated in Fig. 10. As the C/Si ratio is 0:5, the Si_3N_4 phase can

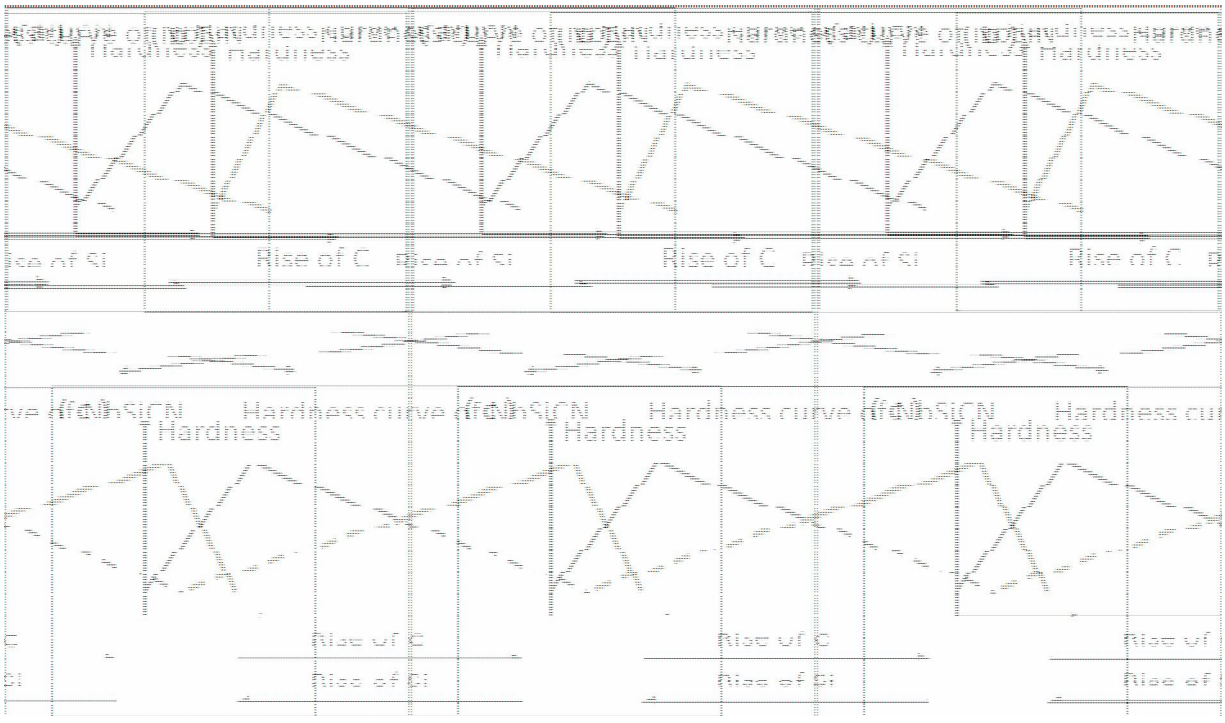

Fig. 9. Schematic illustration of the hardnesses of NbSiCN nanocomposite films with the change of the C/Si content ratio.

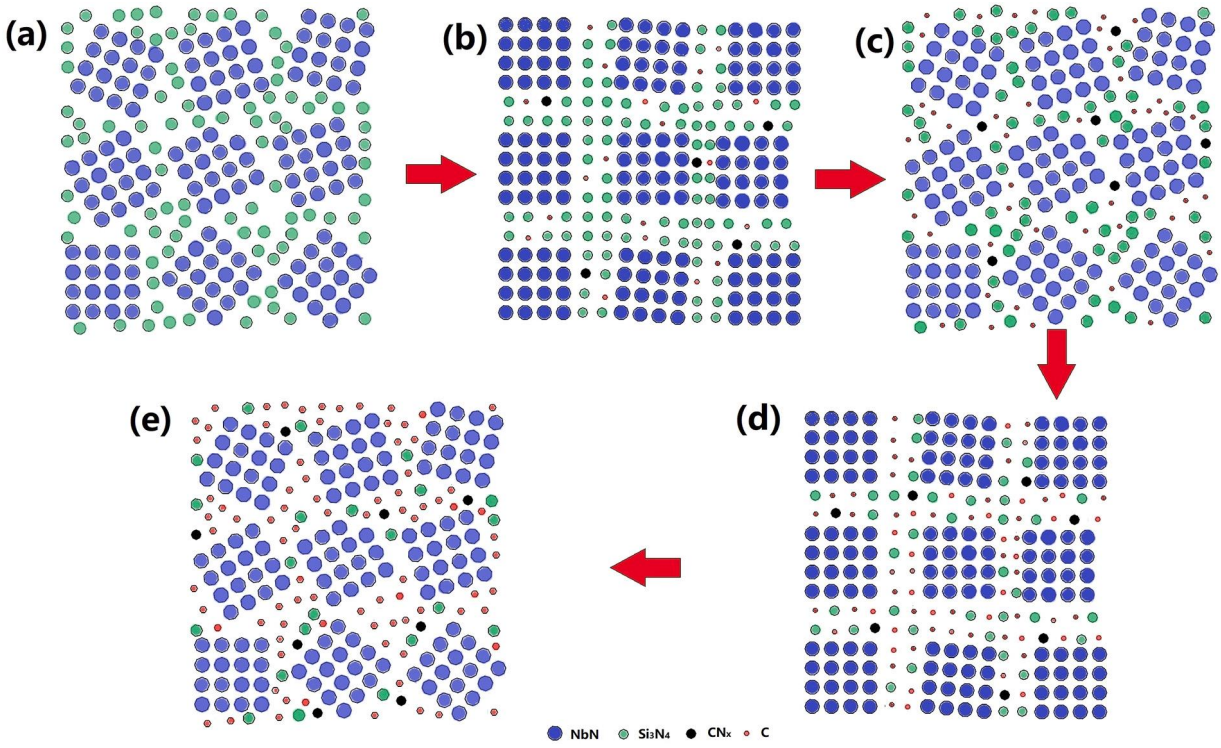

Fig. 10. Schematic illustration of microstructural evolution of NbSiCN nanocomposite films with change of the C/Si content ratio: (a) C/Si = 0:5, (b) C/Si = 1:4, (c) C/Si = 2:3, (d) C/Si = 3:2, and (e) C/Si > 3:2.

segment the NbN nanocrystallite due to the thermodynamic incompatibility between Si_3N_4 and NbN [51]. The Si_3N_4 interface exists in the amorphous state, which damages the coherent interface structure between the Si_3N_4 interface and NbN crystallites, as exhibited in Fig. 10(a). When the C/Si ratio rises to 1:4, due to the addition of the C element, the interface becomes more flexible. In Fig. 10(b), it can be seen that the Si_3N_4/C/CN_x interface inclines to grow a coherent interface with the adjacent NbN nanocrystallites, because of the small interfacial phase thickness. The nanostructure can lower the interfacial energy in the $Nb_{20}Si_4C_1N$ nanocomposite film [23]. The coherent interface structure between the Si_3N_4/C/CN_x interface and NbN crystallites can lead to the amelioration of the film crystallinity, which is in agreement with the XRD results in Fig. 1.

When the C/Si ratio further increases from 1:4 to 2:3, the Si_3N_4/C/CN_x interface cannot keep the coherent interface with the adjacent NbN nanocrystallites, as exhibited in Fig. 10(c). The disappearance of the interface coherency leads to the decrease of the film crystallinity. Meanwhile, without the coherent-interface structure, the hardness effect of the NbSiCN nanocomposite film vanishes away, making for the rapid decrease of the mechanical properties of the NbSiCN nanocomposite film. As the C/Si ratio rises to 3:2, the amounts of C and CN_x exceed Si_3N_4 at interfaces. The change of the chemical composition at the interface leads to the formation of new coherent interface structures between the Si_3N_4/C/CN_x interfaces and NbN crystallites. Meanwhile, a new pronounced preferential orientation of the nanocomposite film forms. Further increasing the C/Si ratio can increase C and CN_x contents at the Si_3N_4/C/CN_x interface. Accordingly, the chemical composition and interfacial energy change, resulting in the disappearance of coherency between the interface and crystallites.

Notably, the remarkable hardness effect is only observed for the $Nb_{20}Si_4C_1N$ and $Nb_{20}Si_2C_3N$ nanocomposite films. From Fig. 1, with the C/Si ratio raises from 1:4 to 3:2, the preferential diffraction peak of the nanocomposite film changes from (200) to (111). The good crystallinity indicates the formation of the interface coherency between interfaces and adjacent nanocrystallites. Meanwhile, the NbN nanocrystallites and interfaces have the different lattice parameters. The interface is subjected to the compressive stress, because of owning the larger lattice parameter. Meanwhile, the NbN nanocrystallite is supposed to endure the tensile stress with the smaller lattice parameter. As a result, the compressive and tensile stress fields are created in the nanocomposite film. According to the alternating-stress theory suggested by Kato et al. [26], the film can be strengthened, due to the blockage of the dislocation motion, by the compressive and tensile stress fields. Moreover, the NbN nanocrystallites and Si_3N_4, C, and CN_x interfaces have totally different shear moduli, which can effectively strengthen the nanocomposite film, based on the modulus-difference theory proposed by Koehler [25].

Intense substrate ion bombardment can lead to residual stress, which during the sputter deposition. The effect of the C/Si ratio on NbSiCN nanocomposite film is shown in Fig. 8. Combined with the results of XRD, and HRTEM, it can be concluded that, the interface coherency intensifies the alternating-stress effect, resulting in residual stress, which may affect the hardness [52–54].

In the field of metallic materials, the Hall-Petch relation is well known to expound the relationship between the yield stress and grain size [55]. Since the dislocation movement is not the main deformation mechanism in the ceramics, there is still some controversy in the validity of the Hall-Petch relation theory [56]. According to the previous studies, the conventional Hall-Petch relationship has been also observed in ceramics [27,28,57–60]. Significantly, the U.S. Naval Research Laboratory revealed the changes in the relative fractions of nanoscale structures in nanocrystalline ceramics, which were published in 2018 [61]. Based on the experimental data in Table 3, two low values of the average crystallite sizes for the nanocomposite films appear on corresponding superhardness films. Thus, the hardness effect of the NbSiCN nanocomposite film could be partially explained by the Hall-Petch relation.

Based on the above analysis, the hardness effect of the NbSiCN nanocomposite films can be explained by the combined effects of the alternating-stress and moduli-difference strengthening mechanisms,

and the Hall-Petch relation theory.

5.3. Theoretical calculations from the coherent-interface-strengthening mechanism

In our previous investigation on NbSiN nanocomposite films [51], the coherent-interface-strengthening mechanism of the NbSiN nanocomposite film has been validated through theoretical calculations. However, the interfacial layer of the NbSiCN nanocomposite film is a $Si_3N_4/C/CN_x$ interfacial layer, rather than being made up of single components. More importantly, under the template effect of adjacent NbN nanocrystallites, the mixed phases of the $Si_3N_4/C/CN_x$ interfacial layer were forced to transform into the fcc structure. However, it is hard to acquire the hardness and elastic modulus of the fcc $Si_3N_4/C/CN_x$ interfacial layer by experiments. Since the fcc-structured interfacial layer is only present as the metastable state, which is inserted in the nanocomposite film, the evaluation of the mechanical properties of the $Si_3N_4/C/CN_x$ interfacial layer is of great importance. For the purpose of accurately evaluating the shear modulus of the fcc $Si_3N_4/C/CN_x$ interfacial layer, the first-principle calculations based on DFT are used to acquire the Young's modulus of the fcc interfacial layer in the $Nb_{20}Si_2C_3N$ nanocomposite film.

Based on the observation and analysis of the XRD patterns in Fig. 1, the diffraction peak of the $Nb_{20}Si_2C_3N$ nanocomposite film is located at the (111) orientation rather than (200) orientation, which can achieve the lowest energy in the fcc structure. In this case, there are two possibilities in the $Nb_{20}Si_2C_3N$ film. One is that the $Nb_{20}Si_2C_3N$ film does not form the nanocomposite structure. The other is that the mismatch rate of the crystal lattices is small between the $Si_3N_4/C/CN_x$ interfacial layer and adjacent NbN nanocrystallite. Meanwhile, the intensity of the (111) diffraction peak reaches the maximum value in the XRD patterns in Fig. 1. Thus, the $Nb_{20}Si_2C_3N$ film possesses the highest crystallization degree in the (111) orientation and forms coherent interfaces. The followed viewpoints can be acquired through the above two phenomena. At first, the $Nb_{20}Si_2C_3N$ nanocomposite film shows the obvious hardness effect with the coherent interface. Secondly, the mismatch rate of the crystal lattices is very small between the $Si_3N_4/C/CN_x$ interfacial layer and adjacent NbN nanocrystallite under the present preparation condition. In the previous studies, the lattice mismatch between the mixed interfacial layer and adjacent nanocrystallite can be generally assumed between 2% and 3% [51,62,63]. Based on the above discussion, the lattice constant of the $Si_3N_4/C/CN_x$ interfacial layer adopts the lattice constant of the fcc-NbN, and it's value is 0.3114 nm.

Fig. 11 reveals the model of the fcc NbN crystal cell. In the present research, the coherent-interface-hardness effect appears in the $Nb_{20}Si_2C_3N$ nanocomposite film. Based on the model of the fcc-structured NbN crystal cell, the model of the fcc-structured $Si_3N_4/C/CN_x$ interfacial layer in $Nb_{20}Si_2C_3N$ can be obtained by replacing

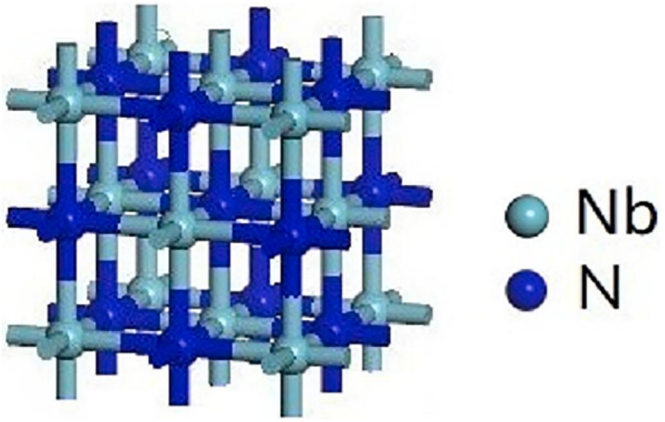

Fig. 11. Model of an fcc-structured NbN crystal cell.

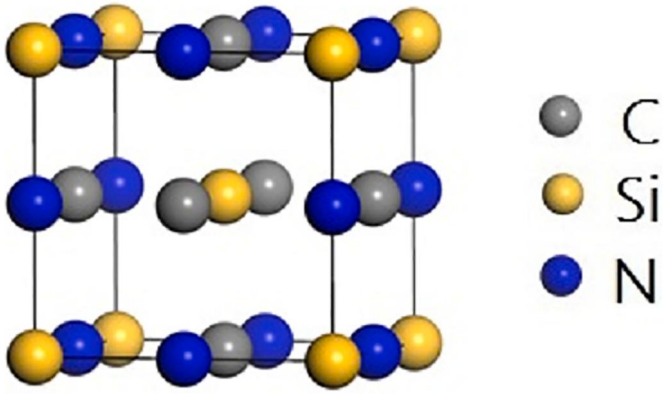

Fig. 12. Model of a $C_9Si_6N_9$ primitive cell.

corresponding atoms in the fcc-structured NbN crystal cell with atoms of carbon and silicon. In the above measurement and analysis, it has been identified that the interface phase is formed of Si_3N_4, C, and trace amounts of CN_x. Therefore, the C/Si content ratio is around 3:2, and the Si/N content ratio is about 3:4 in the interface phase of the $Nb_{20}Si_2C_3N$ nanocomposite film. Moreover, in view of the existence of trace amounts of CN_x, the simplified model of the interface-crystal cell in the $Nb_{20}Si_2C_3N$ nanocomposite film, which can consider the elemental content ratio, is designed as the "$C_9Si_6N_9$" model. For improving the calculation efficiency and considering the effect of the cyclic-boundary condition, it can adopt the most simplified molecular structure to design the molecular structure of the $Si_3N_4/C/CN_x$ interfacial layer. Then in order to acquire the simplified fcc-structured $Si_3N_4/C/CN_x$ interfacial layer, it replaces 6 Nb atoms with 6 Si atoms, and replaces 6 Nb atoms and 3 N atoms with 9C atoms, respectively. Meanwhile, the replacement of atoms is considered as a symmetric distribution of atoms, as shown in Fig. 12.

By means of the simulation calculation on the simplified "$C_9Si_6N_9$" model of the fcc-structured $Si_3N_4/C/CN_x$ interfacial layer in $Nb_{20}Si_2C_3N$, the Young's modulus of the interfacial layer is 401.6 GPa. Through the above simulation, the hardness increment of the $Nb_{20}Si_2C_3N$ nanocomposite film can be calculated in the following methods, respectively, which results from the combined effects of the modulus difference, alternating-stress field, and Hall-Petch relationship. The shear modulus (G) of the interfacial layer in the $Nb_{20}Si_2C_3N$ nanocomposite film can be computed from Eq. (3).

$$G = E/2(1+\nu) \tag{3}$$

where E is the Young's modulus, and ν is the Poisson's ratio. Utilizing the above data for the NbN and interfacial layer in $Nb_{20}Si_2C_3N$ (E_{NbN} = 229 GPa, $E_{C9Si6N9}$ = 401.6 GPa) and the Poisson's ratio of 0.25, the shear moduli of the NbN and interfacial layer in $Nb_{20}Si_2C_3N$ can be calculated as G_{NbN} = 91.6 GPa and $G_{C9Si6N9}$ = 160.6 GPa, respectively.

According to the Koehler's theory [25], the maximum hardness increment of the $Nb_{20}Si_2C_3N$ film, compared with the lower hardness of NbN, can be expressed as follows:

$$\Delta H_{max} = \frac{3RG_B \sin\theta}{8\pi m} \tag{4}$$

where θ is the smallest angle between the interface and the glide plane of the low modulus layer, taking 45° for the $Nb_{20}Si_4C_1N$ nanocomposite film; $R = (G_A - G_B)/(G_A + G_B)$, G_A and G_B are shear moduli of two layers, respectively ($G_A > G_B$, G_A and G_B are thus $G_{C9Si6N9}$ and G_{NbN}, respectively); m, the Taylor factor is 0.3 [64]. Based on the above data, R can be calculated as $R = (G_A - G_B)/(G_A + G_B) = 0.274$. From these data, the hardness increment can be acquired as 7.1 GPa, compared with the NbN.

On the other hand, the hardness increment can be expressed as the

Table 4
Comparison of hardness increments from the modulus-difference theory, alternating-stress-field theory, Hall-Petch relationship, and the experimental value.

Film	Value from modulus- difference theory (GPa)	Value from alternating-stress-field theory (GPa)	Value from Hall-Petch relationship (GPa)	Total theoretical hardness (GPa)	Experimental value of hardness (GPa)
$Nb_{20}Si_2C_3N$	7.1	2.5	3.2	35.4	32.5

following formula, which is according to the alternating-stress-field theory [26].

$$\Delta H \cong 10\tau_{max} = \frac{5\sqrt{6}}{3} A\varepsilon E \quad (5)$$

A is the modulation-amplifying factor influenced by the modulation period, modulation ratio, and roughness and width of interfaces. A takes the value of 0.25 in this calculation according to the studies from Mirkarimi et al. [65] and Shinn et al. [66]. E is the weighted average modulus proportion of the NbSiCN film, and is calculated as 246.3 GPa for the $Nb_{20}Si_2C_3N$ nanocomposite film according to the red dashed line areas in the Fig. 3(c). ε is the lattice mismatch between NbN and Si_3N_4/C/CN_x interfacial phases. Since the Si_3N_4/C/CN_x interfacial phase transforms into a crystalline structure, it is difficult to calculate the lattice mismatch between the NbN and Si_3N_4/C/CN_x interfacial phases. If it is assumed that the lattice mismatch is about 1%, the hardness enhancement is about 2.5 GPa according to Eq. (5).

According to above discussion and previous literatures [27,28], the Hall-Petch relationship can be applied to the NbSiCN nanocomposite films, as follows:

$$H_v = H_0 + k/\sqrt{D} \quad (6)$$

where H_0 and k are determined by the similar ceramic as 17.9 GPa and 21.2 GPa·$nm^{1/2}$ [61], respectively. Based on the above estimated data, the hardness enhancement is about 3.2 GPa.

Combined with the hardness effects obtained from the modulus-difference theory, alternating-stress-field theories, and Hall-Petch relationship, a total hardness increment of about 12.8 GPa can be achieved, relative to NbN (22.6 GPa). Based on the above analysis and calculations, the hardness value of the $Nb_{20}Si_2C_3N$ film can be calculated, which is about 35.4 GPa. The predicted hardness is consistent with the measured value of 32.5 GPa for the $Nb_{20}Si_2C_3N$ nanocomposite film, as shown in Table 4. Therefore, the validity of the coherent-interface-strengthening mechanism has been proved in the NbSiCN nanocomposite film.

6. Conclusions

In conclusion, the hardness effect is found in the NbSiCN nanocomposite films deposited by reactive-magnetron sputtering. The hardnesses and elastic moduli of NbSiCN nanocomposite films depend strongly on the C/Si content ratio and corresponding microstructures. The NbSiCN film is characterized as the nanocomposite structure with the NbN nanocrystallites surrounded by the Si_3N_4/C/CN_x interface phase. The fabrication of the NbSiCN nanocomposite film can be described as a two-way doped mechanism. The variation curve of hardnesses and elastic moduli of NbSiCN films with the different C/Si content ratios shows a “double peak” strengthening feature. Meanwhile, the corresponding $Nb_{20}Si_4C_1N$ and $Nb_{20}Si_2C_3N$ films also show the best crystallinity with the pronounced preferential (200) and (111) orientations, respectively. The interface coherency between the NbN nanocrystallite and interface occurs in the $Nb_{20}Si_4C_1N$ and $Nb_{20}Si_2C_3N$ films. The average crystallite size of the NbSiCN film had an obvious low value, as the C/Si content ratio was 1:4 or 3:2, respectively. The first-principles calculation was utilized to obtain Young's modulus of the interfacial layer, which was difficult to obtain its value by experiments. Accordingly, the combined effects of the modulus-difference theory, alternating-stress-field theory, and Hall-Petch relationship can be used to illustrate the hardness effect of the NbSiCN nanocomposite film.

CRediT authorship contribution statement

Haoming Du: Designing and carrying out the experiments, Writing the article. **Wei Li**: Designing and carrying out the experiments, Writing the article. **Ping Liu**: Supporting the technical activities for the measurements (XRD, HRTEM, and SEM nanoindentation). **Ke Zhang**: Supporting the technical activities for the measurements (XRD, HRTEM, and SEM nanoindentation). **Fengcang Ma**: Supporting the technical activities for the measurements (XRD, HRTEM, and SEM nanoindentation). **Xiaohong Chen**: Supporting the technical activities for the measurements (XRD, HRTEM, and SEM nanoindentation). **Junwei Yang**: Supported the technical activities for the first-principles calculation. **Rui Feng**: Aided with the data analysis. Peter K. Liaw: Aided with the data analysis.

Declaration of competing interest

The authors claim that they have no competing interests.

Acknowledgment

This study was financially supported by the National Natural Science Foundation of China (Grant no. 51471110 and 51971148), the Key Laboratory of Advanced Metal-based Electrical Power Materials (Grant no. 5313310202) of the Shanghai Municipal Commission of Education and Shanghai Engineering Technology Research Center (Grant no. 18DZ2253400). PKL thanks the support from the National Science Foundation (DMR-1611180 and 1809640) with the program directors, Drs. J. Yang, G. Shiflet, and D. Farkas.

Data availability

The raw data required to reproduce these findings cannot be shared at this time as the data also forms part of an ongoing study.

References

[1] A. Niederhofer, T. Bolom, P. Nesladek, K. Moto, C. Eggs, D.S. Patil, S. Veprek, The role of percolation threshold for the control of the hardness and thermal stability of super- and ultrahard nanocomposites, Surf. Coat. Technol. 146-147 (2001) 183–188.
[2] R.A. Andrievski, Nanostructured superhard films as typical nanomaterials, Surf. Coat. Technol. 201 (2007) 6112–6116.
[3] S. Veprek, Recent search for new superhard materials: go nano, J. Vac. Sci. Technol. A31 (2013) 1–33.
[4] S. Veprek, S. Reiprich, S.Z. Li, Superhard nanocrystalline composite materials: the TiN/Si3N4 system, Appl. Phys. Lett. 66 (1995) 2640–2642.
[5] L. Hultman, J. Bareno, A. Flink, H. Soderberg, K. Larsson, V. Petrova, M. Oden, J.E. Greene, I. Petrov, Interface structure in superhard TiN-SiN nanolaminates and nanocomposites: film growth experiments and ab initio calculations, Phys. Rev. B 75 (155437) (2007) 1–6.
[6] M. Kong, W.J. Zhao, L. Wei, G.Y. Li, Investigations on the microstructure and hardening mechanism of TiN/Si3N4 nanocomposite coatings, J. Phys. D. Appl. Phys. 40 (2007) 2858–2863.
[7] W. Li, P. Liu, Y.S. Zhao, F.C. Ma, X.K. Liu, X.H. Chen, D.H. He, New understanding of hardening mechanism of TiN/SiNx-based nanocomposite films, Nanoscale Res. Lett. 8 (427) (2013) 1–7.
[8] W. Li, P. Liu, S. Zhao, K. Zhang, F.C. Ma, X.K. Liu, X.H. Chen, D.H. He, Microstructural evolution, mechanical properties and strengthening mechanism of TiN/Ni nanocomposite film, J. Alloys Compd. 691 (2017) 159–164.

[9] J.F. Wang, Z.X. Song, K.W. Xu, Influence of sputtering bias on the microstructure and properties of Nb-Si-N films, Surf. Coat. Technol. 201 (2007) 4931–4934.
[10] C.S. Sandu, M. Benkahoul, R. Sanjines, F. Levy, Model for the evolution of Nb-Si-N thin films as a function of Si content relating the nanostructure to electrical and mechanical properties, Surf. Coat. Technol. 201 (2006) 2897–2903.
[11] Z.X. Song, Y. Wang, C.J.F. Wang, C.L. Liu, K.W. Xu, The effect of N2 partial pressure on the properties of Nb-Si-N films by RF reactive magnetron sputtering, Surf. Coat. Technol. 201 (2007) 5412–5415.
[12] W. Li, P. Liu, P.K. Liaw, Microstructures and properties of high-entropy alloy films and coatings: a review, Mater. Res. Lett. 6 (2018) 199–229.
[13] J.H. Jeon, S.R. Choi, W.S. Chung, K.H. Kim, Synthesis and characterization of quaternary Ti-Si-C-N coatings prepared by a hybrid deposition technique, Surf. Coat. Technol. 188-189 (2004) 415–419.
[14] S. Abraham, E.Y. Choi, N. Kang, K.H. Kim, Microstructure and mechanical properties of Ti-Si-C-N films synthesized by plasma-enhanced chemical vapor deposition, Surf. Coat. Technol. 202 (2007) 915–919.
[15] A.M. Abd El-Rahman, Ronghua Wei, A comparative study of conventional magnetron sputter deposited and plasma enhanced magnetron sputter deposited Ti-Si-C-N nanocomposite coatings, Surf. Coat. Technol. 241 (2014) 74–79.
[16] Y.J. Kim, H.Y. Lee, T.J. Byun, J.G. Han, Microstructure and mechanical properties of TiZrAlN nanocomposite thin films by CFUBMS, Thin Solid Films 516 (2008) 3651–3655.
[17] T.D. Nguyen, Y.J. Kim, J.G. Han, D.B. Lee, Oxidation of TiZrAlN nanocomposite thin films in air at temperatures between 500 and 700 °C, Thin Solid Films 517 (2009) 5216–5218.
[18] Y.C. Lu, H.W. Chen, C.C. Chang, C.Y. Wu, J.G. Duh, Tribological properties of nanocomposite Cr-Mo-Si-N coatings at elevated temperature through silicon content modification, Surf. Coat. Technol. 338 (2018) 69–74.
[19] J.C. Ding, T.F. Zhang, Q.M. Wang, C.W. Song, T.G. Wang, K.H. Kim, Microstructure and mechanical properties of the Cr-Mo-Si-N nanocomposite coatings prepared by a hybrid system of AIP and HiPIMS technologies, J. Alloys Compd. 740 (2018) 774–783.
[20] J. Xu, G.D. Wang, X.L. Lu, L.L. Liu, P. Munroe, Z.H. Xie, Mechanical and corrosion-resistant properties of Ti-Nb-Si-N nanocomposite films prepared by a double glow discharge plasma technique, Ceram. Int. 40 (2014) 8621–8630.
[21] C. Yan, J.C. Qian, T.W. Ng, Z.F. Zhou, K.Y. Li, W.J. Zhang, I. Bello, Sputter deposition of hard quaternary Al-Mg-B-Ti nanocomposite films, Surf. Coat. Technol. 232 (2013) 535–540.
[22] V. Uvarov, I. Popov, Metrological characterization of X-ray diffraction methods at different acquisition geometries for determination of crystallite size in nano-scale materials, Mater. Charact. 85 (2013) 111–123.
[23] W.C. Oliver, G.M. Pharr, An improved technique for determining hardness and elastic modulus using load and displacement sensing indentation experiments, J. Mater. Res. 7 (1992) 1564–1583.
[24] S. Tamulevicius, Stress and strain in the vacuum deposited thin films fn1, Vacuum 51 (1998) 127–139.
[25] J.S. Koehler, Attempt to design a strong solid, Phys.Rev.B 2 (1970) 547–551.
[26] M. Kato, T. Li, L.H. Schwartz, Hardening by spinodal modulated structure, Acta Metall. 28 (1980) 285–290.
[27] R.W. Rice, Mechanical Properties of Ceramics and Composites: Grain and Particle Effects, M. Dekker, New York, 2000, pp. 233–281.
[28] J.A. Wollmershauser, B.N. Feigelson, E.P. Gorzkowski, C.T. Ellis, R. Goswami, S.B. Qadri, J.G. Tischler, F.J. Kub, R.K. Everett, An extended hardness limit in bulk nanoceramics, Acta Mater. 69 (2014) 9–16.
[29] W. Kohn, L.J. Sham, Self-consistent equations including exchange & correlation effects, Phys. Rev. 140 (1965) A1133–A1138.
[30] P. Hohenberg, W. Kohn, Inhomogeneous electron gas, Phys. Rev. 136 (1964) B864–B871.
[31] D. Vanderbilt, Soft self—consistent pseudopotentials in a generalized eigenvalue formalism, Phys. Rev. B 41 (1990) 7892–7895.
[32] M.D. Segall, P.J.D. Lindan, M.J. Probert, C.J. Pickard, P.J. Hasnip, S.J. Clark, M.C. Payne, First-principles simulation: ideas, illustrations and the CASTEP code, J. Phys. Condens. Matter 14 (2002) 2717–2744.
[33] S.J. Clark, M.D. Segall, C.T. Pickard, P.J. Hasnip, M.J. Probert, K. Refson, M.C. Payne, First principles methods using CASTEP, Z. Kristallogr. 220 (2005) 567–570.
[34] M.C. Payne, M.P. Teter, D.C. Allan, T.A. Arias, J.D. Joannopoulo, Iterative minimization techniques for ab initio total-energy calculations: molecular dynamics and conjugate gradients, Rev. Mod. Phys. 64 (2002) 1045–1097.
[35] H.J. Monkhorst, J.D. Pack, Special points for Brillouin-zone integrations, Phys. Rev. B 13 (1976) 5188–5192.
[36] J.P. Perdew, Y. Wang, Accurate and simple analytic representation of the electron-gas correlation energy, Phys. Rev. B 45 (1992) 13244–13249.
[37] T.H. Fischer, J. Almlof, General methods for geometry and wave function optimization, J. Phys. Chem. 96 (1992) 9768–9774.
[38] Z.X. Song, Y. Wang, C.J.F. Wang, C.L. Liu, K.W. Xu, The effect of N_2 partial pressure on the properties of Nb-Si-N films by RF reactive magnetron sputtering, Surf. Coat. Technol. 201 (2007) 5412–5415.
[39] J.F. Wang, Z.X. Song, K.W. Xu, Influence of sputtering bias on the microstructure and properties of Nb-Si-N films, Surf. Coat. Technol. 201 (2007) 4931–4934.
[40] A.D. Pogrebnjak, O.V. Bondar, G. Abadias, V. Ivashchenko, O.V. Sobol, S. Jurga, E. Coy, Structural and mechanical properties of NbN and Nb-Si-N films: experiment and molecular dynamics simulations, Ceram. Int. 42 (2016) 11743–11756.
[41] N. Saoula, N. Madaoui, R. Tadjine, R.M. Erasmus, S. Shrivastava, J.D. Comins, Influence of substrate bias on the structure and properties of TiCN films deposited by radio-frequency magnetron sputtering, Thin Solid Films 616 (2016) 521–529.
[42] Z.L. Wang, Y. Liu, Z. Zhang, Handbook of Nanophase and Nanostructured Materials, vol. 2, Kluwer Acad. Publishers, New York, 2003, p. 1200.
[43] W.S. Cho, Y.S. Oh, C.S. Kim, M. Osada, M. Kakihana, D.S. Lim, D.S. Cheong, Characterization of Si3N4/SiC nanocomposite by Raman scattering and XPS, J. Alloys Compd. 285 (1999) 255–259.
[44] T. Ujvari, A. Kolitsch, A. Toth, M. Mohai, I. Bertoti, XPS characterizationof the composition and bonding states of the composition and bonding states of elements in CN_x layers prepared by ion beam assisted deposition, Diam. Relat. Mater. 11 (2002) 1149–1152.
[45] Z.L. Fang, Characterization of MOCVD-grown non-stoichiometric SiN_x, Surf. Coat. Technol. 202 (2008) 4198–4203.
[46] S. Badrinarayanan, S. Sinha, X-ray photoelectron spectroscopy studies of the reaction of N_2^+-ion beams with niobium and tantalum metals, Appl. Phys. J. 69 (1991) 1141–1146.
[47] B. Deng, Y. Tao, Z.J. Hu, The microstructure, mechanical and tribological properties of TiN coatings after Nb and C ion implantation, Appl. Surf. Sci. 284 (2013) 405–411.
[48] E. Galvanetto, F.P. Galliano, F. Borgioli, U. Bardi, A. Lavacchi, XRD and XPS study on reactive plasma sprayed titanium-titanium nitride coatings, Thin Solid Films 384 (2001) 223–229.
[49] T. Tharigen, G. Lippold, V. Riede, M. Lorenz, K.J. Koivusarri, D. Lorenz, S. Mosch, P. Grau, R. Hesse, P. Streubel, R. Streubel, R. Szargan, Hard amorphous CSi_xN_y thin films deposited by RF nitrogen plasma assisted pulsed laser ablation of mixed graphite/Si_3N_4-targets, Thin Solid Films 348 (1999) 103–113.
[50] W. Li, P. Liu, Z.H. Xue, F.C. Ma, K. Zhang, X.H. Chen, R. Feng, P.K. Liaw, Microstructures, mechanical behavior and strengthening mechanism of TiSiCN nanocomposite films, Sci. Rep. 7 (2017) 2140.
[51] W. Li, P. Liu, P.C. Chen, K. Zhang, F.C. Ma, X.K. Liu, R. Feng, P.K. Liaw, Microstructure and a coherent-interface strengthening mechanism of NbSiN nanocomposite film, Thin Solid Films 636 (2017) 1–7.
[52] X. Zhang, H. Liang, Z.L. Wu, X.Y. Wu, H.X. Zhang, The effect of substrate bias on titanium carbide/amorphous carbon nanocomposite films deposited by filtered cathodic vacuum arc, Nucl. Instr. Meth. B 307 (2013) 115–118.
[53] A.M. Pagon, E.D. Doyle, D.G. McCulloch, The microstructure and mechanical properties of TiN-Ni nanocomposite thin films, Surf. Coat. Technol. 235 (2013) 394–400.
[54] S.J. Park, K.R. Lee, D.H. Ko, K.Y. Eun, Microstructure and mechanical properties of WC-C nanocomposite films, Diam. Relat. Mater. 11 (2002) 1747–1752.
[55] A.H. Chokshi, On the validity of the hall-petch relationship in nanocrystalline materials, Scr. Metall. 23 (1989) 1679–1684.
[56] A. Krell, Comments on "An extended hardness limit in bulk nanoceramics" by J.A. Wollmershauser, B.N. Feigelson, E.P. Gorzkowski, C.T. Ellis, R. Goswami, S.B. Qadri, J.G. Tischler, F.J. Kub, R.K. Everett, Acta Materialia 69 (2014) 9-16, Scr. Mater. 92 (2014) 63–64.
[57] L.S. Wen, R.F. Huang, L.P. Guo, J. Gong, T.Y. Wei, Y.Z. Chuang, Microstructure and mechanical properties of metal/ceramic Ti/TiN multilayers, J. Magn. Magn. Mater. 126 (1993) 200–202.
[58] J.A. Wollmershauser, B.N. Feigelson, E.P. Gorzkowski, C.T. Ellis, R. Goswami, S.B. Qadri, D.D. Nguyen, J.G. Tischler, F.J. Kub, R.K. Everett, Reply to comments on “An extended hardness limit in bulk nanoceramics”, Acta Materialia 69 (2014) 9-16, Scr. Mater. 92 (2014) 65–68.
[59] R.S. Zhang, H. Wang, M. Tian, Y.Z. Wang, M.Y. Liu, H.M. Wang, G.F. Zhang, Pressureless reaction sintering and hot isostatic pressing of transparent MgAlON ceramic with high strength, Ceram. Int. 44 (2018) 17383–17390.
[60] H.L. Jia, X.J. Liu, Z.X. Li, S.Y. Sun, M. Li, The effect of grain size on the deformation mechanisms and mechanical properties of polycrystalline TiN: a molecular dynamics study, Comput. Mater. Sci. 143 (2018) 189–194.
[61] H. Ryou, J.W. Drazin, K.J. Wahl, S.B. Qadri, E.P. Gorzkowski, B.N. Feigelson, J.A. Wollmershauser, Below the Hall-Petch limit in nanocrystalline ceramics, ACS Nano (2018) 3083–3094.
[62] W. Li, P. Liu, J.T. Wang, F.C. Ma, X.K. Liu, X.H. Chen, D.H. He, Investigation on microstructure and mechanical properties of reactively synthesized TiAlN/AlON nanomultilayers, Vacuum 86 (2012) 1300–1304.
[63] W. Li, P. Liu, K. Zhang, F.C. Ma, X.K. Liu, X.H. Chen, D.H. He, Martensitic transformation of FeNi nanofilm induced by interfacial stress generated in FeNi/V nanomultilayered structure, Nanoscale Res. Lett. 9 (2014) 440.
[64] X. Chu, S.A. Barnett, Model of superlattice yield stress and hardness enhancements, J. Appl. Phys. 77 (1995) 4403–4411.
[65] P.B. Mirkarimi, S.A. Barnett, K.M. Hubbard, T.R. Jervis, L. Hultman, Structure and mechanical properties of epitaxial TiN/V0.3Nb0.7N(100) superlattices, J. Mater. Res. 9 (1994) 1456–1467.
[66] M. Shinn, S.A. Barnett, Effect of superlattice layer elastic moduli on hardness, Appl. Phys. Lett. 64 (1994) 61–63.